Research Square

Preprints are preliminary reports that have not undergone peer review.
They should not be considered conclusive, used to inform clinical practice,
or referenced by the media as validated information.

Characterization of unsteady dynamics and loss mechanisms in supersonic turbine trailing-edge flows

Hugo F. S. Lui

hugolui@unicamp.br

Universidade Estadual de Campinas (UNICAMP)

William R. Wolf

Universidade Estadual de Campinas (UNICAMP)

Research Article

Keywords: Trailing edge flow, supersonic turbine, supersonic base flow, shock-boundary layer interaction, shock-trailing edge interaction

Posted Date: November 13th, 2026

DOI: https://doi.org/10.21203/rs.3.rs-11197611/v1

License: This work is licensed under a Creative Commons Attribution 4.0 International License.
Read Full License

Additional Declarations: No competing interests reported.

Characterization of unsteady dynamics and loss mechanisms in supersonic turbine trailing-edge flows

Hugo F. S. Lui[1*] and William R. Wolf[1]

[1*]Faculdade de Engenharia Mecânica, Universidade Estadual de Campinas, Campinas, 13083-860, São Paulo, Brazil.

*Corresponding author(s). E-mail(s): hugolui@unicamp.br;
Contributing authors: wolf@fem.unicamp.br;

Abstract

This study investigates trailing-edge flow physics in a linear supersonic turbine cascade using wall-resolved large-eddy simulations. Three inlet Mach numbers ($\boldsymbol{M_\infty = 1.85}$, **2.00**, and **2.15**) are considered at a fixed Reynolds number of $\boldsymbol{Re = 395\,000}$ to assess the influence of shock-boundary-layer interactions (SBLIs) on the trailing-edge dynamics. Variations in Mach number shift the SBLIs downstream, causing the suction-side interaction to merge with the trailing-edge recirculation region for $\boldsymbol{M_\infty = 1.85}$ and **2.15**. Cases with an SBLI located near the trailing edge also exhibit amplified pressure fluctuations within the shock–trailing-edge interaction region. Spectral analysis shows that the trailing-edge shocks are dominated by low- and mid-frequency unsteadiness, with increasing Mach number shifting the dominant content toward lower frequencies. Calculation of mass flux over the bubble surface reveals a strongly asymmetric exchange across the trailing-edge separation region, with larger mass-flux magnitudes along the suction-side interface. Temporal correlations indicate that bubble expansions and contractions precede the trailing-edge shock-system response, which is highly synchronized when a large shock-induced separation bubble forms near the trailing edge. Along the wake, increasing Mach number enhances the pressure and density asymmetry between the blade surfaces, which deflects the flow toward the lower-density stream on the suction side. Spectral proper orthogonal decomposition identifies Kelvin-Helmholtz-type coherent structures at higher frequencies along the wake, with similar modal topologies for all cases. Finally, entropy-generation analysis shows that viscous dissipation dominates the aerodynamic losses, primarily within the suction-side boundary layer, whereas the wake contributes only a minor fraction.

Keywords: Trailing edge flow, supersonic turbine, supersonic base flow, shock-boundary layer interaction, shock-trailing edge interaction

1 Introdution

The flow past a blunt turbine trailing edge can be characterized by several features, including flow separation, shear-layer development, turbulent mixing, shock waves, and wake formation. These phenomena strongly influence the aerodynamic performance, entropy generation, heat transfer, and structural integrity of the blade [1, 2]. Consequently, several authors have investigated the trailing-edge flow physics for turbines operating in subsonic and transonic regimes using both experimental and numerical approaches [3–10]. In contrast, studies focusing on the supersonic regime remain scarce, and the underlying flow physics in this

operating condition are not yet fully understood. Nevertheless, supersonic fluid machinery presents promising advantages for size and cost reductions in high-speed propulsion and power-generation systems [11].

In turbomachinery guide vanes operating in a supersonic regime, the interaction between the suction (convex) and pressure (concave) surface boundary layers at the trailing edge generates complex flow dynamics, exhibiting features typical of supersonic base flows. The blunt geometry of the trailing edge forces these approaching boundary layers to separate, forming upper and lower shear layers above and below the recirculation bubble (the base region). These shear layers ensure a smooth and continuous transition between the inner subsonic recirculating flow and the outer supersonic flows, with the associated flow deflections generating compression waves that coalesce into trailing-edge shock waves. Downstream, the upper and lower shear layers converge toward the wake centerline to form a unified mixing layer.

The complex interaction of dual supersonic streams downstream of blunt-base geometries has been extensively investigated using both experimental methods [12–21] and numerical simulations [22–27]. Among these experimental investigations, Herrin and Dutton [12] examined the supersonic near-wake of an axisymmetric cylindrical afterbody at a uniform freestream Mach number of 2.5. Contrary to the historically assumed "dead-air" hypothesis, their measurements revealed significant reverse flow speeds, reaching up to 27% of the freestream velocity, accompanied by high turbulence intensity within the recirculation bubble. Herrin and Dutton [13] subsequently expanded on this work by comparing the near-wake flowfields of blunt and boat-tailed cylinder afterbodies. They observed that incorporating a boat-tail led to a substantial recovery in base pressure that ultimately reduced total base drag by 21%. Furthermore, their findings indicated that higher turbulence intensity levels within the shear layer correlate with a decrease in base pressure. They attributed this phenomenon to intensified fluid mass entrainment, where the shear layer draws more fluid mass from the recirculation region and, consequently, reattaches further upstream.

Subsequent experimental work by Scarano and Van Oudheusden [15] examined a two-dimensional blunt base at a freestream Mach number of 2.0. Turbulent flow measurements showed pronounced streamwise turbulence intensity along the developing shear layers, which peaked near the reattachment region as a result of shear layer merging. Humble et al. [17] conducted PIV measurements on a two-dimensional blunt base across three incoming Mach numbers (1.46, 1.78, and 2.27). Their results demonstrated that increasing the Mach number shifts the reattachment location upstream while causing both the expansion fan and oblique shock waves to incline more sharply toward the wake centerline. From a computational perspective, Simon et al. [22] performed numerical simulations of a compressible mixing layer past an axisymmetric trailing edge at a freestream Mach number of 2.46. Spectral analysis of the separated flow and shear layer identified low-frequency unsteadiness, which the authors linked to the breathing motion (contraction and expansion) of the recirculation bubble alongside shear layer flapping.

Stack [26] performed high-fidelity simulations to examine the influence of splitter plate thickness on near-wake dynamics separating two supersonic turbulent streams under non-equal flow conditions. For the full-thickness and half-thickness cases, the authors observed the presence of large-scale, spanwise-coherent rollers in the wake, whereas the one-tenth-thickness case exhibited coherent rollers only near the trailing edge prior to their breakdown into fine-scale turbulence downstream. For all thicknesses studied, the mixing layer consistently deflected toward the lower-density stream. Regarding turbulent structures in axisymmetric configurations, Kirchner et al. [20] experimentally investigated a longitudinal cylinder wake at Mach 2.49.

Their results highlighted the role of shear layer vortex orientation: upright hairpin vortices reduced spatial shear-layer growth rates, thereby reducing fluid mass entrainment from the recirculation region, which in turn displaced the reattachment location downstream and increased base pressure, whereas inverted hairpin vortices induced the opposite behavior.

The majority of previous research on supersonic base flows has considered configurations in which the incoming boundary layer develops over flat surfaces. However, curved walls are inherent to turbomachinery blades, and they are influenced by the local pressure gradient and streamline curvature, which in turn affect the state of the approaching boundary layer prior to reaching the trailing edge. To account for these effects, the present work investigates the physics of trailing-edge flow in a supersonic turbine cascade using wall-resolved large-eddy simulations and post-processing techniques. Three inlet Mach numbers are analyzed in the cascade, $M_\infty = 1.85$, 2.00, and 2.15 at a fixed Reynolds number $Re = 395\,000$ based on the axial chord and inlet velocity. These inflow variations allow us to examine how the location of the shock-boundary-layer interactions (SBLIs) over the blade influence the trailing-edge flow dynamics.

The remainder of this work is organized as follows: Section 2 describes the numerical methodology and flow configurations analyzed. Section 3 presents the flow field analysis, beginning with instantaneous structures in Section 3.1 and mean flow statistics in Section 3.2. Next, a spectral analysis of the shock waves and separation bubble in the trailing-edge region is performed in Section 3.3 to characterize their relevant flow frequencies. Sections 3.4 and 3.5 examine the mass flux across the trailing-edge bubble surface and the temporal correlations between bubble breathing and trailing-edge shocks, respectively, providing insight into the coupled dynamics of the separation region and shock system. The wake dynamics are investigated in Section 3.6 using spectral proper orthogonal decomposition to identify coherent structures and their characteristic frequencies. Finally, Section 3.7 analyzes the sources of entropy generation in the supersonic turbine, followed by the main conclusions in Section 4.

2 Flow configuration and numerical methodology

Wall-resolved large-eddy simulations (LES) of a linear cascade of supersonic turbines are carried out as described by Lui et al. [28, 29], and an overview of the flow configuration and numerical methodology is provided here. The vane geometry, as well as the fluid properties and inflow conditions, follow those used by Liu et al. [30], being summarized in Fig. 1(a). In the present study, however, the inlet Mach number is varied by prescribing a uniform inflow at three values: $M_\infty = 1.85$, 2.00, and 2.15. The Reynolds number based on the inlet velocity u_{inlet} and the axial airfoil chord c_x is fixed at $Re = 395\,000$. The fluid is considered as a calorically perfect gas with a ratio of specific heats $\gamma = 1.31$, Prandtl number $Pr = 0.747$, and the ratio of the Sutherland constant over the inlet temperature $S_\mu/T_\infty = 0.07182$.

The non-dimensional compressible Navier-Stokes equations are solved in a curvilinear coordinate system. An overset mesh approach is used, comprising two overlapping grids: a body-fitted O-grid that accurately resolves the turbulent boundary layers around the blade, and an H-grid that facilitates the application of pitchwise periodicity in the cascade. In both grid blocks, spatial discretization is performed using a sixth-order compact finite-difference scheme implemented on a staggered grid [31]. A sixth-order compact interpolation scheme is employed to evaluate flow quantities at the required staggered-grid locations. At each

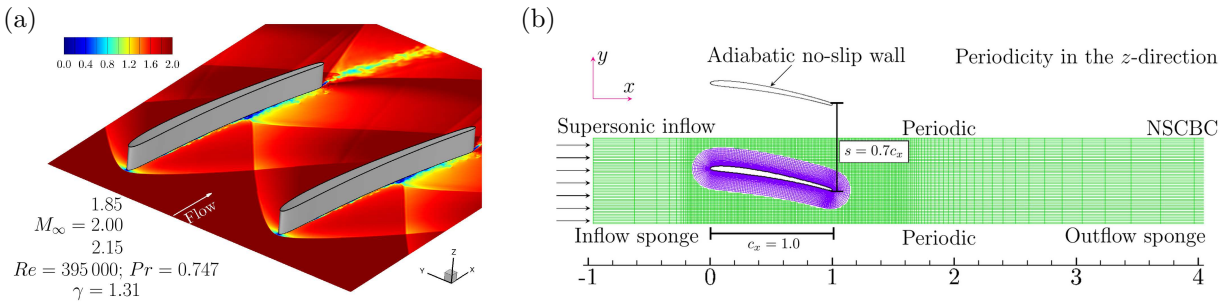


Fig. 1: Overview of the computational setup: (a) Mach number contours of three-dimensional cascade geometry with inflow conditions; (b) computational domain and boundary conditions, with every fifth grid point displayed.

time step, a sixth-order compact filter [32] is applied in regions away from solid boundaries to suppress high-wavenumber numerical instabilities associated with mesh non-uniformities and overset-grid interpolations.

No explicit subgrid-scale model is used in the present calculations; instead, the high-order compact filter provides an implicit approximation to such modeling [33]. To introduce only minimal numerical dissipation near shock waves, sufficient to maintain numerical stability, while avoiding excessive damping of turbulent scales, the localized artificial diffusivity (LAD) scheme LAD-D2-0 [34] is employed to compute additional artificial bulk viscosity and thermal conductivity, which are then added to their physical counterparts. Time integration in the O-grid block is performed using an implicit second-order scheme to mitigate the stiffness associated with the fine boundary layer resolution, whereas a third-order Runge–Kutta method is applied in the H-grid block. Data exchange between the overlapping grids is achieved using a fourth-order compact interpolation procedure. Additional information on the governing equations, non-dimensionalization procedure, and the LES numerical methodology is available in Nagarajan et al. [31], Bhaskaran and Lele [35], and Lui et al. [29].

Although turbine blades are typically subjected to inflow turbulence, a uniform supersonic inflow is prescribed at the inlet. This allows a direct comparison against canonical SBLI configurations studied in the literature. Transition to turbulence in the airfoil boundary layers is triggered using a body-force formulation that mimics a tripping device [29, 36]. The trip is implemented as an unsteady forcing composed of random spanwise disturbances with an amplitude selected to induce bypass transition. It is applied over a wall-normal extent $0 < \Delta n < 0.001c_x$ at $0.22 < x < 0.27$ on the suction side, and over the same wall-normal distance at $0.10 < x < 0.15$, on the pressure side. At the outlet, a Navier–Stokes characteristic boundary condition (NSCBC) [37] is applied. Damping sponge layers are included near both the inflow and outflow boundaries to absorb convected numerical disturbances [31]. Adiabatic no-slip conditions are enforced on the airfoil surface. To model a linear cascade of vanes, pitchwise periodicity is imposed in the y-direction of the background grid, and spanwise periodicity is applied to both grid blocks. Details regarding the boundary conditions and computational grid are provided in Fig. 1(b).

For all simulations, the O-grid block uses $1280 \times 300 \times 144$ points in the streamwise, wall-normal, and spanwise directions, respectively. The background Cartesian grid has $960 \times 280 \times 72$ points. In total, the computational mesh contains approximately 75×10^6 points. In the present simulations, the grid resolution follows the standard recommendations for wall-resolved LES [38]. Chordwise distributions of grid spacing in wall units, as well as the ratio between the local grid spacing and the Kolmogorov length scale, are provided in

Ref. [28]. The spanwise domain size corresponds to 10% of the axial chord, which is equivalent to 7 incoming boundary layer thickness on the suction side for the $M_\infty = 2.15$ case (thickest boundary layer computed for all cases). This value is comparable to or larger than those used in most high-fidelity computations [39–42]. Furthermore, two-point spanwise correlations of tangential and normal velocity fluctuations at several chord locations, presented in Lui et al. [28], confirm that the chosen spanwise extent is sufficient and does not constrain the turbulence dynamics.

3 Results

After an initial transient period, simulation data are collected for approximately 45 nondimensional time units (based on the inlet velocity and axial chord) to compute the flow statistics for different inlet Mach numbers of a supersonic turbine cascade. This dataset allows the evaluation of the trailing-edge flow physics in the present base flow configurations through flow visualizations, mean flow and spectral analyzes of the trailing-edge shock system and separation bubble, modal decomposition of the wake flow, mass-flux assessment over the separation bubble, and quantification of entropy generation over the entire turbine blade.

3.1 Instantaneous flow features through the turbine cascade

To contextualize the present investigation of trailing-edge flow dynamics, the key flow features of the supersonic cascade reported in [28, 29, 43] are briefly summarized below. Instantaneous flowfields for different inlet Mach numbers are shown in Fig. 2. The turbulent boundary layers are depicted by isosurfaces of Q-criterion colored by streamwise velocity, with separated flow regions highlighted in blue. The shock waves are visualized on a background plane of density gradient magnitude $\|\nabla\rho\|$. Detached bow shocks formed at the airfoil leading edges develop into oblique shocks that impinge on the turbulent boundary layers of adjacent blades. These SBLIs impose adverse pressure gradients that induce flow separation bubbles. On the suction side, the impinging oblique shock interacts with the turbulent boundary layer; however, unlike canonical interactions over flat plates or compression ramps, the upstream compression waves do not coalesce into a distinct separation shock. On the pressure side, a Mach reflection occurs, resulting in a thin recirculation bubble despite the severe pressure jump across the normal shock.

The curved walls of the airfoils significantly influence the SBLIs by modifying the upstream boundary layer development and local pressure fields [28, 44]. Prior to shock impingement, the suction-side boundary layer evolves along a convex surface, subjecting it to a favorable pressure gradient and bulk dilatation. In contrast, the concave curvature of the pressure side imposes an adverse pressure gradient and bulk compression on the incoming boundary layer. Furthermore, variations in the inlet Mach number shift the shock impingement location, modulating the strength and spatial extent of these curvature-induced effects. As the inlet Mach number increases, the shock impingement locations and resulting SBLIs progressively shift downstream on both airfoil sides. At $M_\infty = 1.85$, two distinct SBLIs develop on the suction side due to the leading-edge bow shock and the reflected shock from the adjacent pressure side. In contrast, only a single suction-side SBLI occurs at $M_\infty = 2.00$ and 2.15. For $M_\infty = 2.15$, the downstream displacement of the SBLI causes the interaction to occur sufficiently close to the trailing edge, merging the shock-induced separation bubble with the trailing-edge separated flow, yielding a complex coupled separation topology. As discussed by Lui et al. [28], the observed discrepancies in separation bubble size (between the suction and

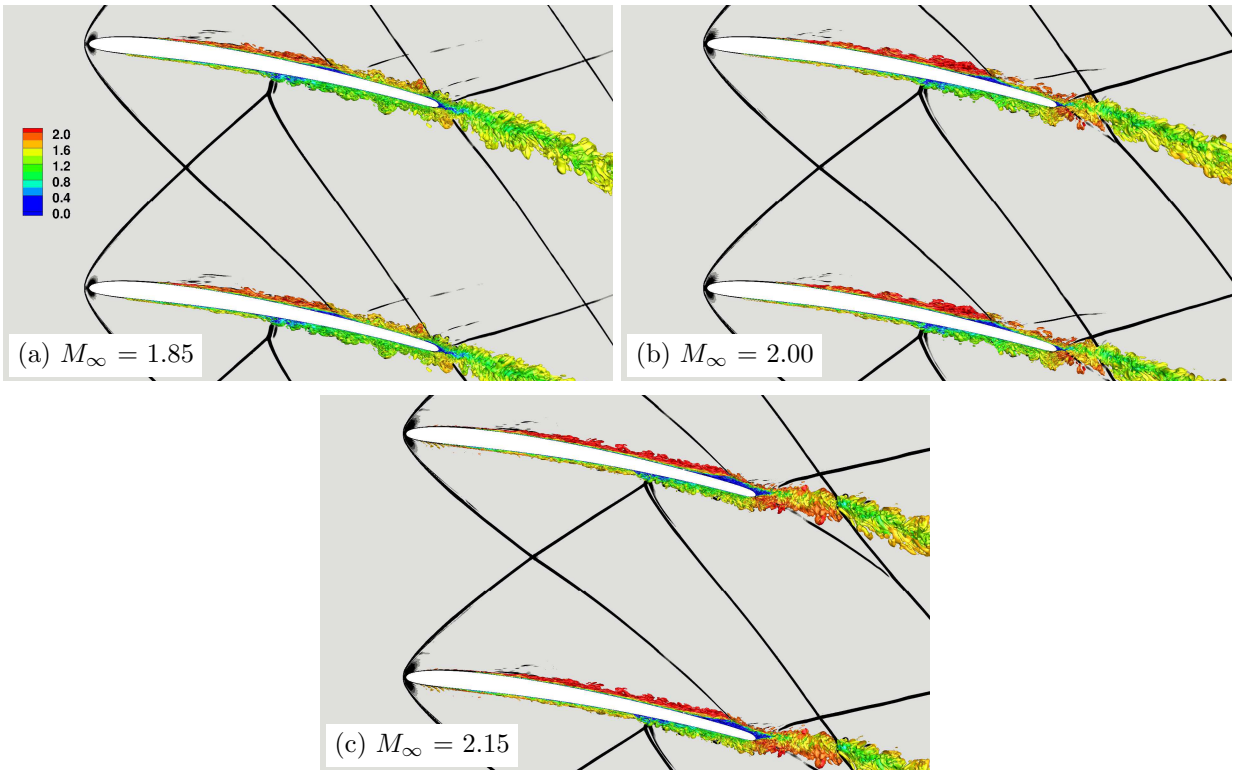


Fig. 2: Instantaneous flowfields for different inlet Mach numbers. The plots show isosurfaces of Q-criterion colored by the streamwise velocity component (u/a_∞), with background contours of density gradient magnitude $\|\nabla\rho\|$.

pressure surfaces, and across the various inlet Mach numbers) stem from the combined effects of upstream pressure gradients, bulk dilatation, and near-wall turbulent kinetic energy (TKE) levels within the upstream boundary layer.

3.2 Mean flow and turbulence characteristics in the trailing-edge region

To highlight the trailing-edge flow topology, including the effects of inlet Mach number, the spanwise and time-averaged contours of the streamwise velocity component are shown on the left-hand side of Fig. 3. Here, the values are normalized by the inlet speed of sound. Regions enclosed by white lines indicate separation bubbles, while dashed and solid black lines denote the sonic line and shock/expansion waves, respectively. As the supersonic boundary layers along the suction (convex) and pressure (concave) surfaces interact at the trailing edge, the flow develops characteristics typical of supersonic base flows and planar mixing layers. The blunt trailing-edge geometry induces separation of the approaching boundary layers, generating upper and lower shear layers on either side of the recirculation bubble. Farther downstream, these shear layers deflect and converge toward the wake centerline, merging to form a single mixing layer. This deflection of the flow is driven by compression waves that coalesce into shock waves at the trailing edge.

Regarding the effects of the inlet Mach number on flow topology, SBLIs occur closer to the trailing edge of the suction side for both $M_\infty = 1.85$ and $M_\infty = 2.15$. In both cases, the shock-induced separation bubble merges (in the mean sense) with the trailing-edge bubble, resulting in a small separation region at $M_\infty = 1.85$ and a large recirculation region at $M_\infty = 2.15$. In these cases, the free shear layer formed

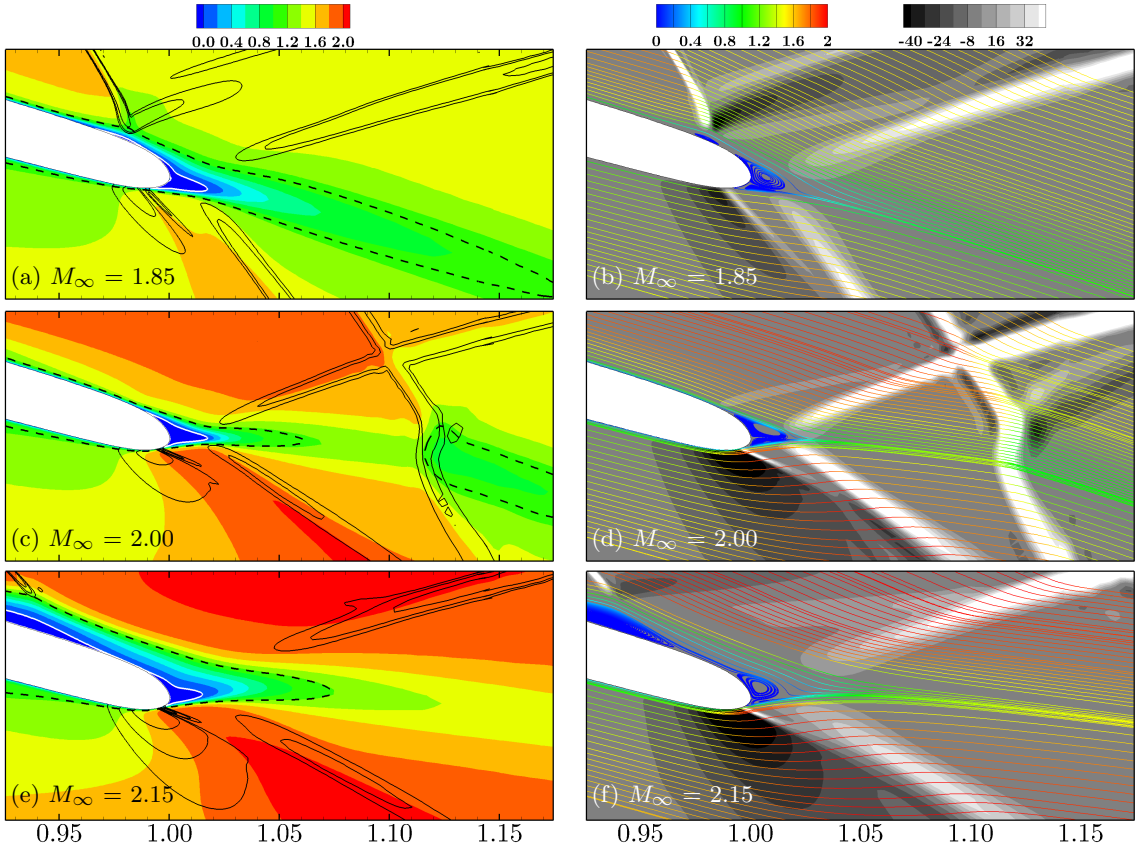


Fig. 3: Spanwise and time-averaged contours of the streamwise velocity component u/a_∞ (left) and $\boldsymbol{U} \cdot \nabla p$ superimposed by streamlines colored by u/a_∞ (right) for different Mach numbers. In the left column, the white lines depict the separation bubbles, while the dashed and solid black lines show the sonic lines and shock/expansion waves, respectively.

downstream of the incident shock becomes the structure that ensures a continuous variation of the flow between the trailing-edge separation region and the outer supersonic freestream flow. As a result, the upper shear layer thickness increases, with the effect being more pronounced for $M_\infty = 2.15$. In the mean sense, the reverse flow within the trailing-edge bubble reaches up to 8%, 10%, and 7% of the freestream velocity for $M_\infty = 1.85$, $M_\infty = 2.00$, and $M_\infty = 2.15$, respectively. The subsonic flow regions near the trailing edge are strongly influenced by variations in the inlet Mach number. At $M_\infty = 1.85$, the wake remains locally subsonic, permitting both upstream- and downstream-propagating waves. In the other two cases, the wake starts subsonic, accelerates to supersonic speeds, and then returns to subsonic flow with an accompanying deflection due to downstream shock-turbulence interactions (omitted for $M_\infty = 2.15$ for visual clarity, but shown in Fig. 2(c))

The right-hand panels of Fig. 3 display contours of $\boldsymbol{U} \cdot \nabla p$ to highlight shock and expansion waves. This quantity is negative (dark regions) during flow expansion and positive (light regions) during compression. In addition, streamlines colored by the streamwise velocity component are overlaid to illustrate the wake trajectory. As previously noted, when an SBLI occurs near the trailing edge of the suction side, a thicker upper shear layer develops. This displaces the sonic line away from the bubble, which consequently shifts the upper trailing-edge shock outward as well. On the pressure side near the trailing edge, the flow undergoes

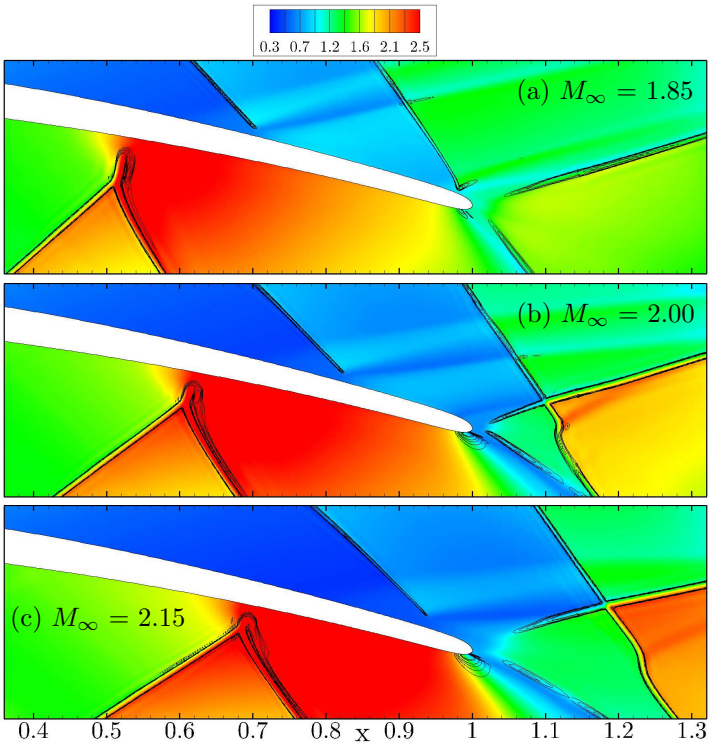


Fig. 4: Contours of spanwise- and time-averaged normalized pressure (p/p_{inlet}) across inlet Mach numbers. Shock waves are indicated by black isolines of pressure gradient magnitude, $\|\nabla p\|$.

stronger expansion as the inlet Mach number increases. Downstream of these expansion waves, a weak compression wave, commonly termed a lip shock, forms at the separation point to balance the pressure between the supersonic outer stream and the separated flow. A suction-side lip shock is also observed for the $M_\infty = 2.00$ case. Increasing the inlet Mach number also causes the lower trailing-edge oblique shock to incline more steeply toward the wake centerline, consistent with findings for planar base flows by Humble et al. [17].

To assess the influence of turbine passage pressure fields on wake deflection, Fig. 4 presents spanwise- and time-averaged pressure contours normalized by the inlet value, with shock waves visualized by isolines of pressure gradient magnitude $\|\nabla p\|$. Increasing the inlet Mach number shifts the SBLIs downstream on both suction and pressure sides and amplifies the pressure and density differences near the trailing edge. This occurs because the suction-side boundary layer develops under a favorable pressure gradient while the pressure-side boundary layer is subjected to an adverse pressure gradient; therefore, the downstream displacement of the SBLI leads to a reduced pressure jump on the suction side and an increased jump on the pressure side. For the $M_\infty = 1.85$ case, the appearance of the second SBLI on the suction side equalizes the pressure between the suction and pressure surfaces near the trailing edge, thereby preventing wake deflection. In contrast, the higher Mach number cases exhibit pronounced pressure asymmetry, resulting in a deflection of the wake toward the lower-pressure (lower-density) side, as evidenced in Figs. 2 and 3. Similar behavior has been reported in the literature of high-speed mixing layers [26, 45, 46].

Figure 5 presents the wall distributions of normalized flow quantities along the trailing edge for different inlet Mach numbers, using the inlet values as reference. A local coordinate system along the trailing edge is

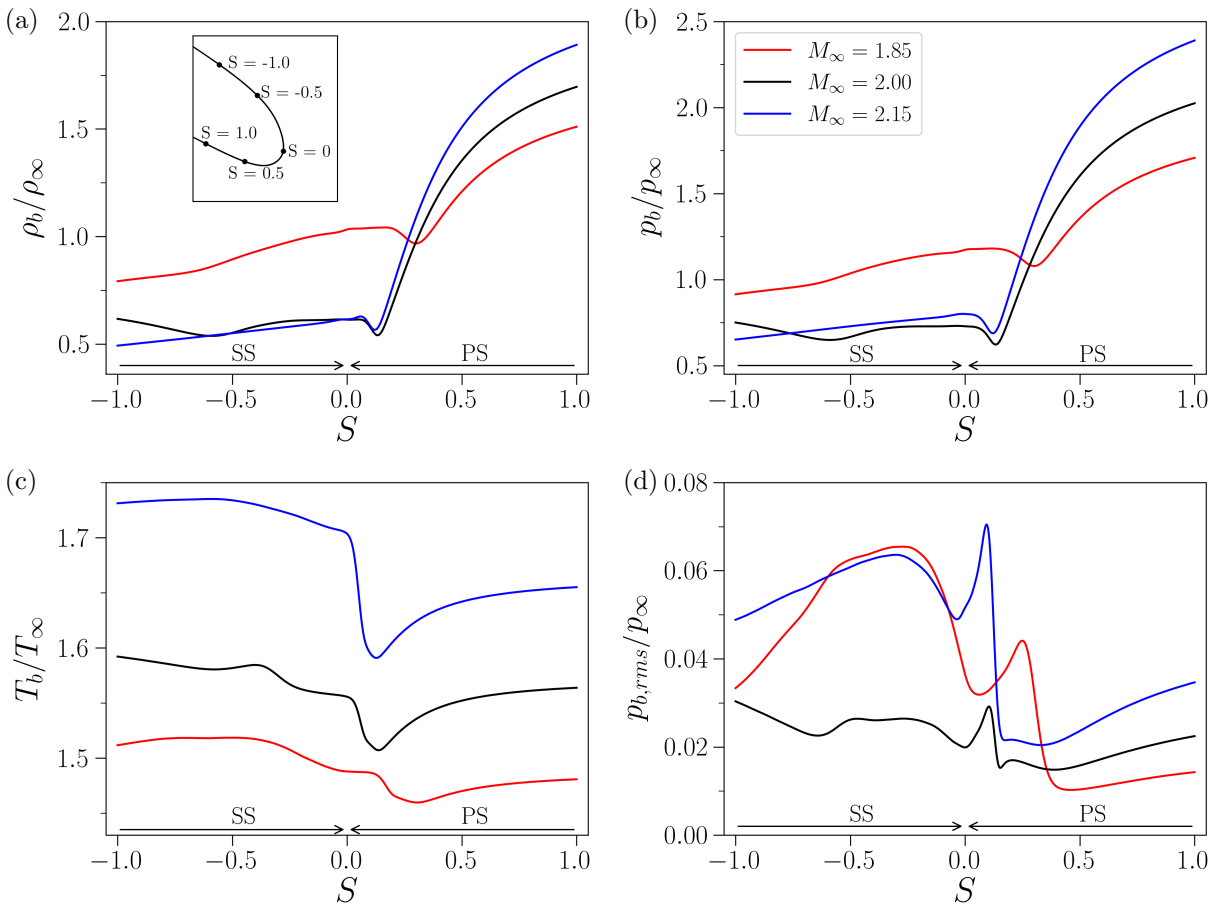


Fig. 5: Spanwise and time-averaged normalized (a) base density ρ_b, (b) base pressure p_b, (c) base temperature T_b, and lastly (d) the RMS of normalized base pressure $p_{b,rms}$. The inset shows the new coordinate system along the trailing edge. The suction side (SS) distributions appear on the left of $S = 0.0$, while those on the pressure side (PS) are shown to the right. Note that the outer flow is essentially right to left for the PS, as indicated by the black arrow.

parameterized by the curvilinear coordinate S (see inset), where $S < 0$ and $S > 0$ correspond to the suction side (SS) and pressure side (PS), respectively ($S = 0$ marks the trailing-edge apex). The normalized base density ρ_b/ρ_∞ in Fig. 5(a) confirms that, in the mean sense, higher inlet Mach numbers amplify the density difference between the suction and pressure sides near the trailing edge, consistent with the mean pressure flow fields in Fig. 4. The normalized base pressure p_b/p_∞ is displayed in Fig. 5(b). On the pressure side, expansion waves induce a large pressure drop upstream of the trailing edge, followed by a mild pressure rise across the lip shock (Fig. 3). On the suction side, the SBLI occurring near the rear section of the airfoil for $M_\infty = 1.85$ and $M_\infty = 2.15$ imposes an adverse pressure gradient. In contrast, for the $M_\infty = 2.00$ case, a favorable pressure gradient develops downstream of the SBLI, as discussed by Hamada et al. [44], until a lip shock causes a slight compression, downstream of which a characteristic pressure plateau develops along the trailing-edge separation bubble.

The normalized base temperature T_b distribution is displayed in Fig. 5(c). Higher inlet Mach numbers increase wall temperatures due to enhanced viscous dissipation within the boundary layer [47]. Furthermore, the temperature rise induced by the pressure-side lip shock intensifies with increasing inlet Mach number.

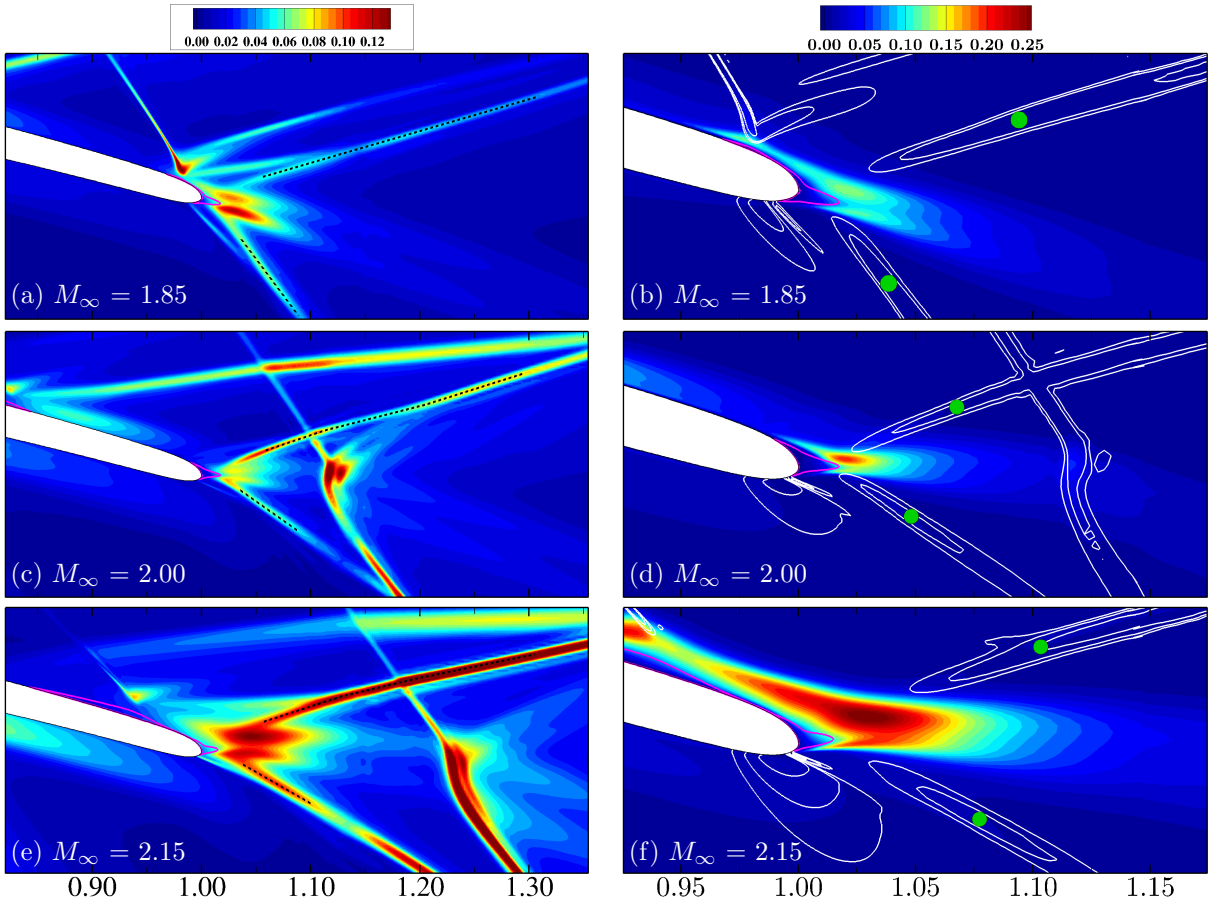


Fig. 6: Root-mean-square values of pressure (left) and turbulent kinetic energy (right) for different inlet Mach numbers. The white lines indicate the shock and expansion waves, visualized using the pressure-gradient magnitude. The separated flow regions are shown in magenta. Black dashed lines in the left-column panels indicate the probe locations used for the spectral analysis of the trailing-edge shocks. The green circles indicate the probe locations used for the time-correlation analysis.

Figure 5(d) shows the root-mean-square (RMS) of the normalized base pressure. Across all cases, the RMS pressure peaks near the pressure-side lip shock, with substantially higher peak amplitudes observed when an SBLI occurs near the trailing edge ($M_\infty = 1.85$ and $M_\infty = 2.15$). These trailing-edge SBLIs also markedly amplify wall pressure fluctuations along the suction-side rear section compared to the non-interacting baseline case ($M_\infty = 2.00$).

To characterize the unsteady dynamics in the near-wake region and the trailing-edge shock system, the distributions of root-mean-square (RMS) pressure fluctuations and turbulent kinetic energy (TKE) are analyzed in Fig. 6 over different inlet Mach numbers. In each subfigure, the mean recirculation regions are delineated by magenta lines. For all cases, pronounced pressure RMS levels are observed along the trailing-edge shocks. High pressure RMS values also occur within the shear layers near the shock foot, with the highest peaks developing when an SBLI takes place near the trailing edge. Distinct flow features emerge for individual cases. In the $M_\infty = 1.85$ case, elevated pressure RMS levels appear within the suction-side SBLI region, specifically along the incident shock emanating from the adjacent airfoil pressure surface and along the reattachment compression waves. In addition, the lower shear layer exhibits higher pressure fluctuations

than the upper shear layer. For $M_\infty = 2.00$ and $M_\infty = 2.15$, significant pressure fluctuations also develop within the shock-wake interaction region. Overall, the $M_\infty = 2.15$ case, which features an SBLI resulting in a large separation bubble, displays the highest RMS values over the trailing-edge region.

Contours of turbulent kinetic energy (TKE) are presented in Figs. 6(b), (d), and (f). In these subfigures, the shock waves are indicated by white lines. In all cases, elevated TKE levels develop along the shear layers, with peak values localized in the upper shear layer, particularly downstream of the trailing-edge bubble, where shear layers of opposite spanwise vorticity merge. Downstream of this confluence region, TKE decays monotonically as the wake recovers, consistent with previous base-flow investigations [15, 17, 26]. Increasing the inlet Mach number amplifies TKE levels both within the shear layers and throughout the near wake. Moreover, both the $M_\infty = 1.85$ and $M_\infty = 2.15$ cases begin to experience an amplification of TKE values near the rear end of the airfoil's suction side due to the free shear layer generated by the SBLI near the trailing edge [48].

3.3 Spectral analysis of trailing-edge shock system and separation-bubble dynamics

To examine the unsteadiness of the trailing-edge shocks, the power spectral density (PSD) maps obtained from pressure probes along the upper (left panels) and lower (right panels) shocks are shown in Fig. 7. The probe locations are indicated by the black dotted lines in the left panels of Fig. 6. The PSDs are calculated using Welch's method, in which the time signals are divided into four segments with a 66% overlap, and a Hann window is applied to mitigate edge discontinuities. The frequency is nondimensionalized in terms of two Strouhal numbers based on different characteristic length scales: $St_c = fc_x/U_\infty$, based on the axial chord, and $St_{te} = fd_{te}/U_\infty$, based on the trailing-edge thickness. For the present configuration, the trailing-edge thickness d_{te} is approximately $0.02c_x$. Therefore, to obtain St_{te} from St_c, St_c must be multiplied by 0.02. Both Strouhal numbers use the inlet velocity U_∞ as the characteristic velocity. The PSD contours are plotted on a logarithmic scale, with the contour ranges chosen to highlight the most energetic spectral content for each case.

For the $M_\infty = 1.85$ case, the upper trailing-edge shock displays high spectral energy content across $St_c \approx 0.30$–2.00 ($St_{te} \approx 0.008$–0.040), with distinct peaks near $St_c \approx 0.50$, 0.70, 1.20, and 1.80. In addition, a weak, very-low-frequency signature is present around $St_c \approx 0.08$–0.15 ($St_{te} \approx 0.001$–0.003). For the lower trailing-edge shock, high spectral energy is found in a range similar to that of the upper shock, with the most energetic frequencies located at $St_c \approx 2.00$–3.00 ($St_{te} \approx 0.045$–0.060). For the $M_\infty = 2.00$ case, the PSD of the upper trailing-edge shock exhibits high-amplitude energy concentrated in the range $St_c \approx 0.45$–0.60 ($St_{te} \approx 0.009$–0.012), along with noticeable spectral content at $St_c \approx 1.20$ ($St_{te} \approx 0.025$). Where the shock originating from the pressure side of the adjacent blade intersects the upper trailing-edge shock (see Fig. 6 at $x \approx 1.10$), very-low-frequency fluctuations ($St_c \approx 10^{-2}$–10^{-1}) are excited. Furthermore, downstream of $x \approx 1.20$, the most energetic frequencies are significantly amplified, and a low-frequency content emerges across $St_c \approx 10^{-2}$–10^{-1}. This behavior is likely associated with the proximity of the upper trailing-edge shock to the reattachment shock from the SBLI, as observed in Fig. 6. Regarding the lower trailing-edge shock, significant spectral energy is found across the range $St_c \approx 0.40$–4.00 ($St_{te} \approx 0.008$–0.080), with two dominant peaks visible at $St_c \approx 0.50$ ($St_{te} \approx 0.010$) and $St_c \approx 2.00$ ($St_{te} \approx 0.040$).

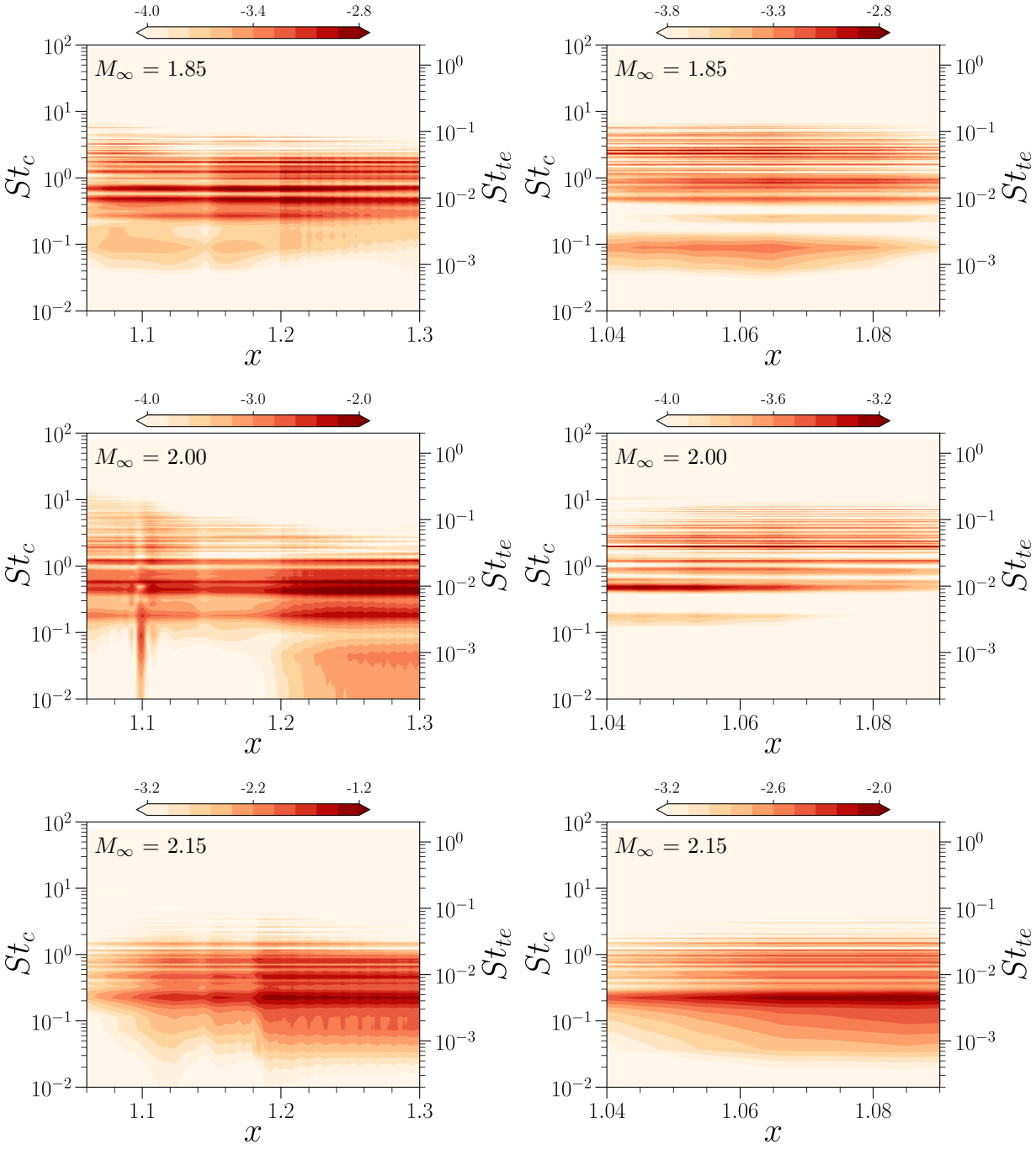


Fig. 7: Power spectral density maps of pressure probes along the upper (left) and lower (right) trailing-edge shocks for different inlet Mach numbers. The probe locations are indicated by black dotted lines in Fig. 6.

For the $M_\infty = 2.15$ case, high spectral energy along the upper trailing-edge shock is distributed across $St_c \approx 0.20$–1.00 ($St_{te} \approx 0.004$–0.020), exhibiting distinct peaks at $St_c \approx 0.25$, 0.50, and 0.80. Downstream of the intersection with the shock originating from the pressure side of the adjacent blade (at $x \approx 1.18$), the spectral energy at these frequencies is significantly amplified, as shown in Fig. 6. For the lower trailing-edge shock, elevated spectral energy spans a frequency range similar to that of the upper shock, with dominant frequencies concentrated at $St_c \approx 0.20$–0.30 ($St_{te} \approx 0.004$–0.006). Overall, increasing M_∞ from 1.85 to

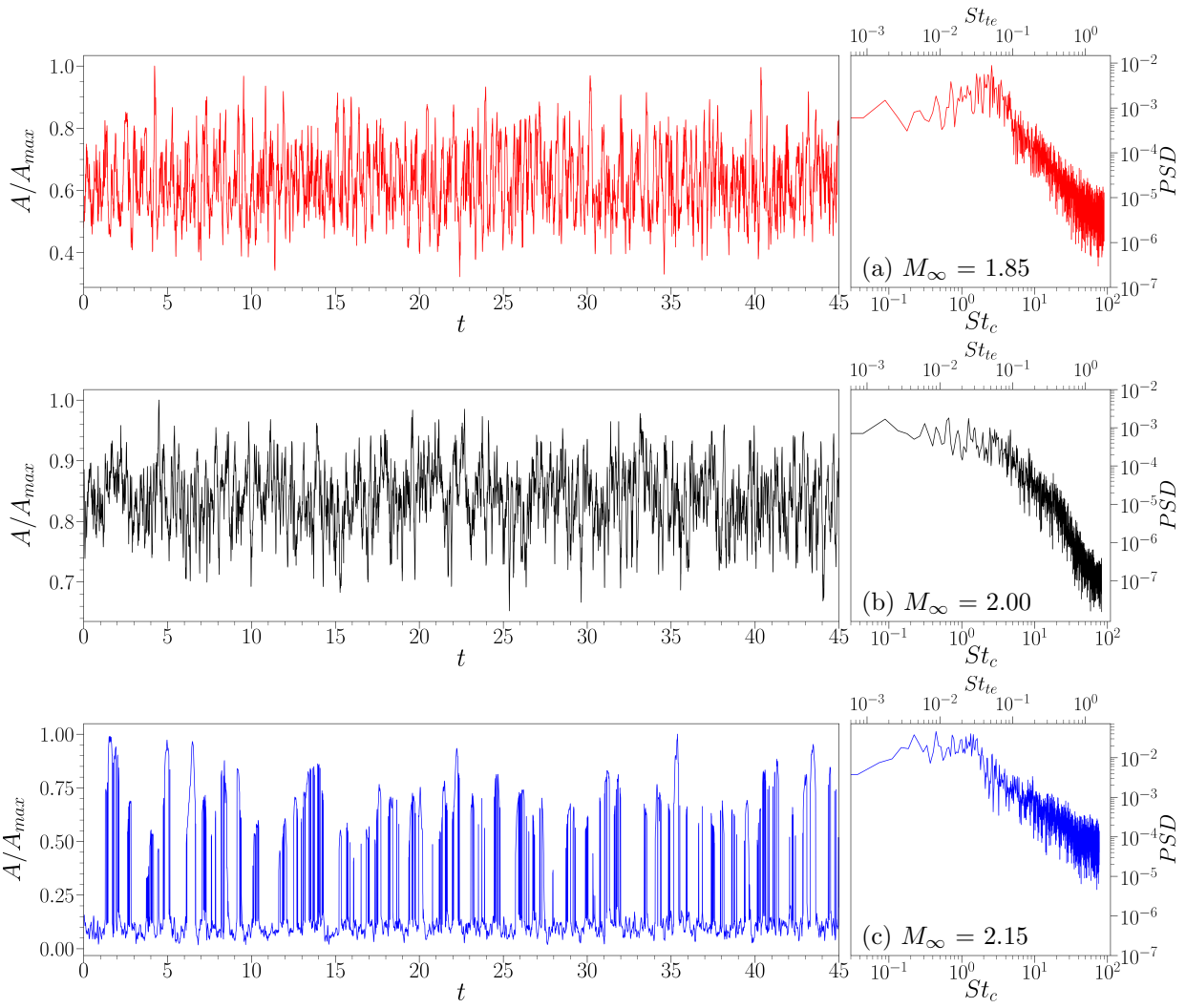


Fig. 8: Spectral analysis of the bubble area for different inlet Mach numbers. The left panel shows the temporal signal, while the right panel shows the corresponding PSDs.

2.15 systematically shifts the dominant shock unsteadiness toward lower frequencies, an effect particularly evident along the lower trailing-edge shock. This behavior could be related to the larger separation bubble formed near the trailing edge at $M_\infty = 2.15$. In addition, the PSD magnitude increases monotonically with Mach number across both shocks, indicating stronger pressure oscillations that agree with the pressure RMS distributions in Fig. 6. Furthermore, the results reveal that key energetic peaks along the upper trailing-edge shock are consistent with the characteristic frequencies associated with the suction-side SBLI bubble, especially for the $M_\infty = 2.00$ and 2.15 cases [28]. Moreover, the fluctuation amplitudes of the upper trailing-edge shocks are consistently higher than those of the lower trailing-edge shocks, indicating that the former exhibit a more pronounced unsteady dynamics.

To investigate the unsteadiness of the trailing-edge bubble, the time evolution of the bubble area normalized by its maximum value and its corresponding PSD are presented in Fig. 8 for all Mach numbers. Here, the bubble is defined as the region enclosed by the contour line of $u = 0$. The signals reveal that in the cases where an SBLI occurs near the trailing edge ($M_\infty = 1.85$ and 2.15), the trailing-edge bubble undergoes stronger expansion and contraction. This occurs due to the merging of the SBLI-induced bubble

on the suction side and the trailing-edge bubble. This merging effect is significantly more intense for the $M_\infty = 2.15$ case, where the bubble dynamics exhibit an intermittent behavior driven by the large difference in size between the two bubbles. Specifically, when these regions merge, the trailing-edge bubble expands drastically, whereas it remains small when they separate.

The PSD analysis reveals that the characteristic frequencies of the trailing-edge bubble are sensitive to inlet Mach number. For the $M_\infty = 1.85$ case, the most energetic fluctuations are concentrated in the mid-frequency range, exhibiting a dominant peak at $St_c \approx 3.00$. Interestingly, this frequency does not emerge as a dominant peak in the spectral signatures of the upper and lower trailing-edge shocks shown in Fig. 7. At $M_\infty = 2.00$, the dominant spectral energy shifts to the low-frequency range, with prominent peaks observed at $St_c \approx 0.09$, 0.30, 0.45, 0.60, and 1.25. Several of these frequencies (e.g., $St_c \approx 0.45$, 0.60, and 1.25) correspond to those of the suction-side SBLI [28] and the upper trailing-edge shock. Similarly, for $M_\infty = 2.15$, the unsteadiness is governed by low-frequency dynamics, featuring dominant peaks at $St_c \approx 0.25$, 0.50, and 0.80. These frequencies also correspond to those excited by the suction-side SBLI [28], as well as with the spectral signatures of the upper and lower trailing-edge shocks shown in Fig. 7. These results indicate that both the bubble dynamics and the trailing-edge shock waves are directly influenced by upstream features of the SBLI, with this effect becoming more pronounced at the higher Mach numbers considered.

3.4 Mass flux over the trailing-edge bubble surface

To investigate the mass entrainment and ejection within the trailing-edge separation bubbles for all Mach numbers, the mass flux is computed along the bubble surface as

$$m'' = \rho(\vec{V_r} \cdot \vec{n}) \ , \tag{1}$$

where $\vec{V_r}$ is the local fluid velocity relative to the bubble surface and $\vec{n}$ is the normal vector pointing outward from the surface. The mass flux is evaluated following the procedure presented by Lui and Wolf [43], which adapts the methodology commonly used to calculate local entrainment velocities across turbulent/non-turbulent interfaces [49, 50]. Figure 9 shows the time-averaged normalized mass flux m'' along the trailing-edge bubble (top plots) and the mean u-velocity flow fields in the trailing-edge region (bottom plots) for different inlet Mach numbers.

For all cases, higher inflow and outflow mass fluxes are observed along the upper part of the trailing-edge bubble (suction side), indicating that mass exchange across its interface is strongly asymmetric. Along the suction-side interface, mass leaving the bubble (positive values of m'') predominantly occurs near the airfoil trailing-edge apex ($x = 1.0$). Farther downstream, m'' changes sign, and mass entering the bubble (negative values of m'') becomes dominant as the flow approaches the downstream closure point. Despite the changes in size and shape of the trailing-edge separation region with inlet Mach number, all cases exhibit a similar spatial organization of mass flux, characterized by ejection in the upstream portion of the suction-side interface followed by entrainment near the downstream closure. Along the pressure-side interface, the opposite trend is observed, although with lower magnitudes of m''. To better visualize the trailing-edge bubble dynamics, Movies 1, 2, and 3, corresponding to $M_\infty = 1.85$, 2.00, and 2.15, respectively, show the mass injection and ejection along the bubble surface and are provided as Supplementary Material.

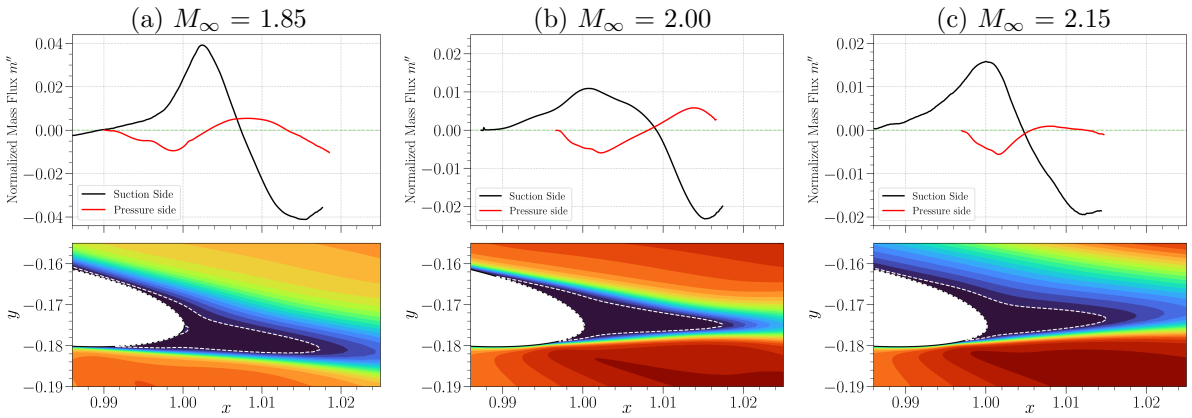
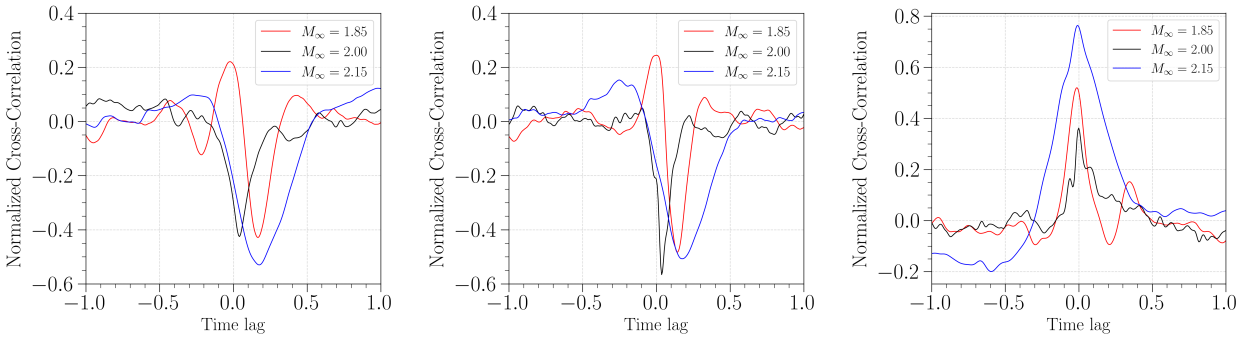


Fig. 9: Normalized mass flux m'' along the trailing-edge bubble surface for different inlet Mach numbers (top panels) and mean u-velocity fields in the trailing-edge region (bottom panels), with the bubble interface indicated by the white dashed line corresponding to the $u = 0$ contour.

3.5 Time correlations between the trailing-edge separation bubble and shocks

To investigate the relationship between the trailing-edge bubble dynamics and the motion of the trailing-edge shocks, Fig. 10 shows the time correlations between (a) the bubble area and the upper shock, (b) the bubble area and the lower shock, and (c) the upper and lower shocks. The temporal signals associated with the upper and lower shocks are obtained from pressure probes located at the respective shock locations, as indicated by the green circles in Fig. 6. The results indicate a clear relationship between the trailing-edge bubble dynamics and the unsteadiness of the trailing-edge shocks.



(a) Bubble area and upper shock (b) Bubble area and lower shock (c) Upper and lower shocks

Fig. 10: Time correlations between the trailing-edge bubble area and the pressure signals measured at the upper and lower trailing-edge shocks for different inlet Mach numbers.

For all Mach numbers, the bubble-area signal exhibits a pronounced negative correlation with both the upper and lower shock pressure signals, with the largest correlation magnitudes occurring at relatively small positive time lags. Since the bubble-area signal is used as the reference, the positive time lag indicates that variations in the shock signals follow changes in the bubble area. When the bubble expands, the shocks move downstream, causing the pressure at the probe locations to decrease; the opposite occurs when the bubble contracts. This behavior indicates that the trailing-edge shock system is dynamically coupled to

the breathing of the separation bubble, with the shock response lagging the bubble-area fluctuations. In contrast, the upper and lower shock signals are positively correlated, with a pronounced peak close to zero time lag. Large correlation values are observed for the cases in which an SBLI occurs near the trailing edge. The correlation is particularly strong for $M_\infty = 2.15$, where a large shock-induced separation bubble forms near the trailing edge, indicating a highly synchronized motion of the two trailing-edge shocks. This result is consistent with the spectral analysis presented in Fig. 7, in which both shocks exhibit very similar spectral content and energetic peaks.

3.6 Spectral modal decomposition of coherent structures in the wake

Spectral proper orthogonal decomposition (SPOD) is employed to identify coherent structures and their characteristic frequencies in the wake [51]. The modal analysis is performed over a total sampling duration of 45 flow-through times, with the data partitioned into eight segments using a 75% overlap and a Hann window. To properly account for compressibility effects, the inner product is defined based on the Chu energy norm [52], which incorporates kinetic and thermal fluctuations into a single measure of perturbation energy. Figure 11 presents the normalized SPOD energy spectrum of the leading mode across different inlet Mach numbers. The eigenvalues are normalized by the total flow energy integrated over all frequencies, such that the area under each curve reflects the fractional energy captured by the first mode, which accounts for approximately 65% to 72% of the total fluctuating energy depending on the Mach number. In addition, Fig. 12 displays the SPOD spatial modes of the v-velocity component computed over a domain restricted to the trailing-edge region (light-blue area). The selected frequencies (magenta dots in Fig. 11) are chosen based on their energy levels and distinct spatial support to prevent plotting redundant mode shapes.

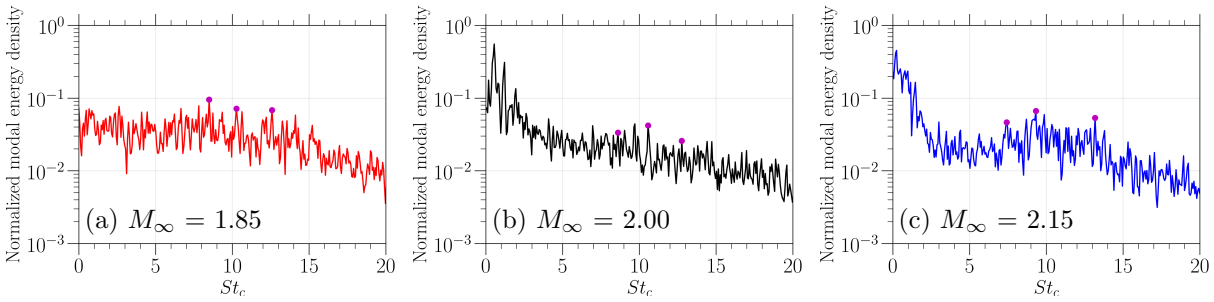


Fig. 11: Normalized SPOD energy spectrum across different inlet Mach numbers. The magenta dots indicate the selected frequencies used to compute the SPOD spatial modes.

The SPOD energy spectrum plots reveal that the majority of the modal energy is concentrated in the lower-frequency range ($St_c < 2.0$) for $M_\infty = 2.00$ and 2.15, whereas the spectrum displays a more broadband distribution for $M_\infty = 1.85$. This lower-frequency content is associated with the trailing-edge shocks, as shown in Fig. 7. Furthermore, the SPOD analysis indicates that the wake-flow dynamics are governed by higher frequencies ($St_c > 7$). At these selected frequencies, the corresponding SPOD spatial modes reveal organized, alternating wave packets that originate immediately downstream of the trailing-edge separation bubble (highlighted by the green-shaded area). The spatial organization of these structures is consistent with a shear-layer instability of Kelvin–Helmholtz type, with the resulting coherent motions convecting

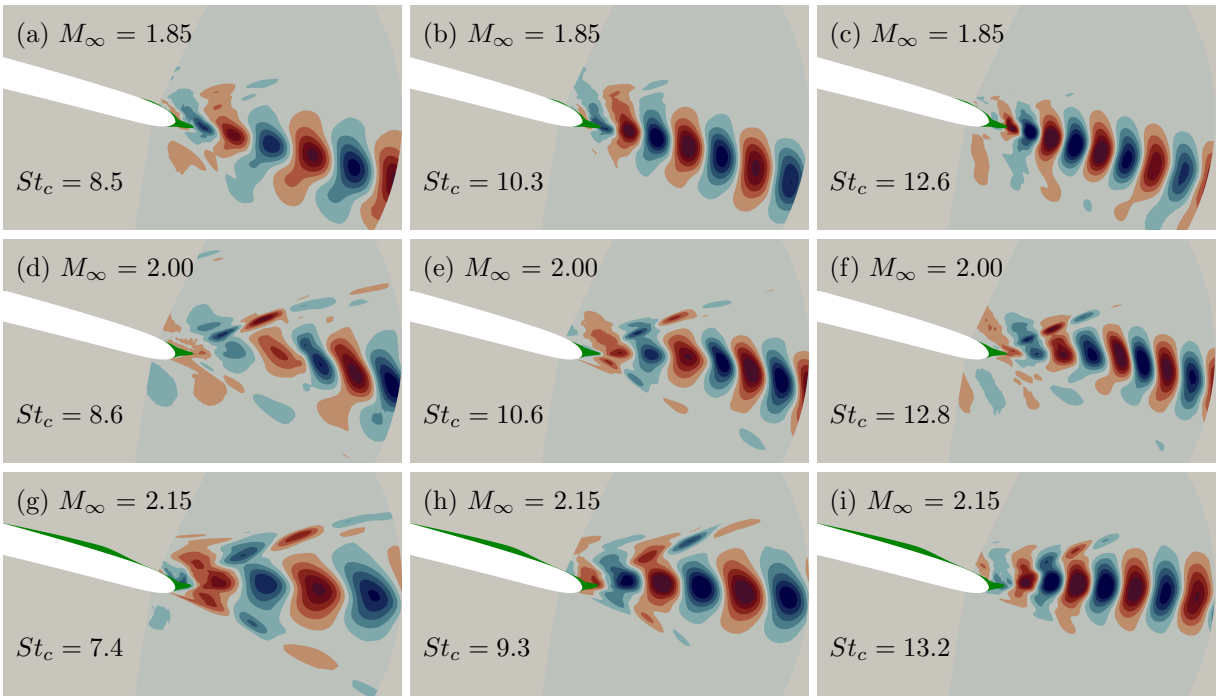


Fig. 12: SPOD spatial modes in the trailing-edge region at selected wake-flow frequencies across different inlet Mach numbers. The green-shaded area indicates the separation bubble

downstream into the wake, as commonly observed in near-wake flows [17, 26, 53, 54]. As the frequency increases, the coherent structures exhibit shorter streamwise wavelengths. In general, the topology of the wake modes is preserved across the different Mach numbers, suggesting that the fundamental instability mechanism remains robust within the investigated regime. However, a shift in the orientation of the wake deflection toward the suction side is evident as M_∞ increases, consistent with the earlier analysis of the mean flowfields.

3.7 Entropy Generation

To investigate the sources of entropy generation in the present supersonic turbine cascade at different inlet Mach numbers, the entropy transport equation is examined. This equation is derived by combining the Gibbs relation, the kinetic energy equation, and the internal energy equation for a fluid element [55]:

$$\frac{\partial(\rho s)}{\partial t} + \nabla \cdot \left(\rho \boldsymbol{U} s - \frac{M_\infty \mu}{RePr} \frac{\nabla T}{T} \right) = \underbrace{\frac{1}{T} \frac{M_\infty}{Re} \boldsymbol{\tau} : \nabla \boldsymbol{U}}_{\Phi} + \underbrace{\frac{M_\infty \mu}{RePr} \frac{(\nabla T)^2}{T^2}}_{\Upsilon} . \tag{2}$$

The equations are written in a nondimensional form, using the procedure presented by Lui et al. [29]. Here, s is the entropy, $\boldsymbol{U}$ is the velocity vector, $\boldsymbol{\tau}$ is the viscous stress tensor, and μ is the dynamic viscosity. The first term on the left-hand side of Eq. 2 represents the time rate of change of entropy per unit volume at a fixed point, and the terms in parentheses on the same side are associated with the entropy flux due to mass and heat fluxes. The right-hand side of Eq. 2 corresponds to the entropy source terms due to viscous dissipation of kinetic energy Φ and irreversible heat transfer Υ. Figure 13 presents the spatial distribution

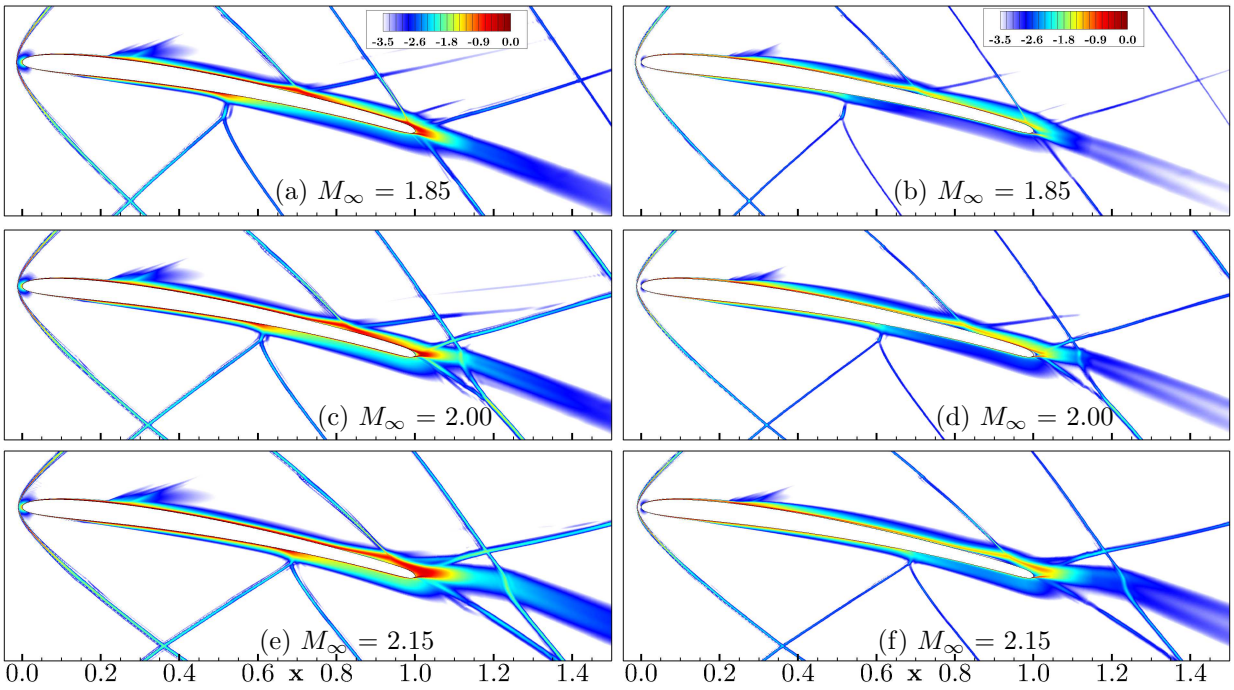


Fig. 13: Contours of spanwise- and time-averaged nondimensional entropy generation rate per unit volume due to viscous dissipation Φ (left) and irreversible heat transfer Υ (right) for different inlet Mach numbers. The contours are plotted on a $\log_{10}$ scale for better visualization.

of the entropy source terms per unit volume. The left and right panels display the viscous dissipation Φ and the irreversible heat transfer Υ terms, respectively.

For all Mach numbers, viscous dissipation is the dominant source of entropy generation. This is corroborated by comparing the results in Fig. 13 with those in Fig. 14, which present contours of the spanwise- and time-averaged non-dimensional total entropy generation rate per unit volume ($\Phi + \Upsilon$). Elevated values of Φ appear within the boundary layers, shear layers and wake. While the spatial distribution of the irreversible heat conduction term is similar to that of the viscous dissipation term, its magnitude is consistently lower. In high-speed flows, the kinetic energy of the flow is substantial, leading to severe velocity gradients along shock structures and near-wall regions. The mechanical energy dissipated by these intense shear stresses naturally outweighs the entropy produced by thermal diffusion, especially for a case with an adiabatic wall [47].

Figure 15 quantitatively presents the spanwise- and time-averaged entropy generation rate per unit volume, segmented by both flow regions and entropy source terms. The first observation from Fig. 15(a) is that the total entropy generation increases monotonically with the inlet Mach number. Regarding the entropy generation in each region of the flow, the suction side (SS) acts as the primary driver of aerodynamic losses, accounting for approximately 50% to 58% of the total entropy generated across all Mach regimes. The pressure side (PS) represents the second most significant contribution, yielding roughly 35% to 38% of the total losses, whereas the wake region accounts for a comparatively minor fraction, ranging from 6% to 12%. A detailed decomposition of these irreversibilities is illustrated in Fig. 15(b). Across all regions and Mach numbers, viscous dissipation (Φ) overwhelmingly dictates the entropy generation when compared to irreversible heat transfer (Υ), as previously observed in Fig. 13.

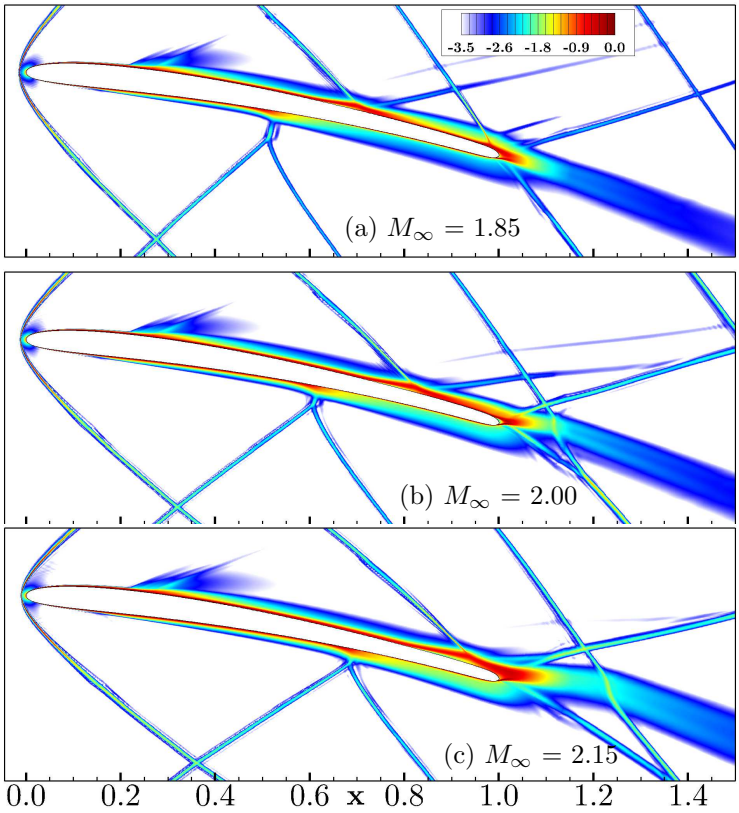


Fig. 14: Contours of spanwise- and time-averaged nondimensional total entropy generation rate per unit volume ($\Phi + \Upsilon$) for different inlet Mach numbers. The contours are plotted on a $\log_{10}$ scale for better visualization.

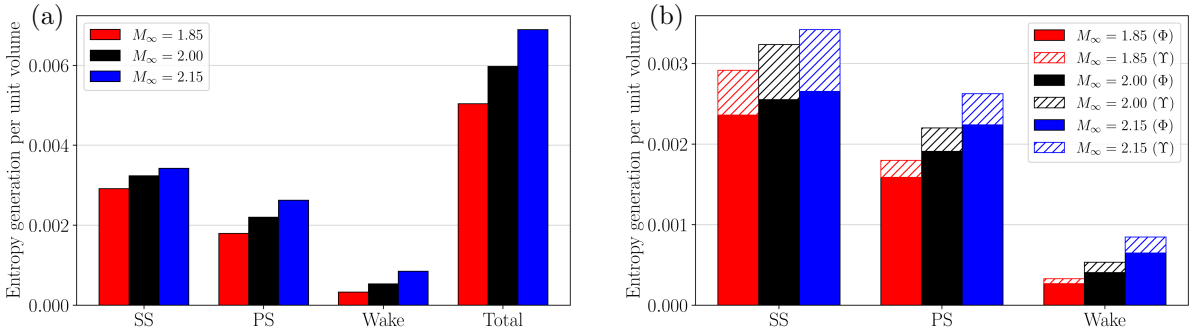


Fig. 15: Quantitative breakdown of the entropy generation per unit volume in the suction side (SS), pressure side (PS), and wake regions for different Mach numbers. (a) Total entropy generation rate ($\Phi + \Upsilon$) and (b) decomposition of the entropy generation into its constituent source terms: viscous dissipation (Φ, solid bars) and irreversible heat transfer (Υ, hatched bars).

These findings exhibit both similarities and key distinctions when compared to entropy source term analyses in subsonic turbines [56–58]. Across both flow regimes, viscous dissipation dominates irreversible heat transfer along the vane boundary layers, with the suction side remaining the dominant source of

entropy generation. However, the entropy generation in the wake region diverges: while it is substantial in the subsonic regime relative to the blade surfaces, it accounts for a comparatively minor fraction in the supersonic regime, even with trailing-edge shock waves present. This disparity is most likely associated with the much steeper velocity gradients within the supersonic boundary layers, which cause viscous losses along the surface to dominate over downstream wake contributions.

4 Conclusions

The present work investigates the physics of the trailing-edge flow in a linear supersonic turbine cascade using wall-resolved large-eddy simulations and post-processing techniques. Three inlet Mach numbers ($M_\infty = 1.85$, 2.00, and 2.15) are analyzed at a fixed Reynolds number of $Re = 395\,000$, based on the axial chord and inlet velocity. These inflow variations enable the detailed examination of how the location of the SBLI over the airfoil influences the trailing-edge flow dynamics, particularly the near-wake flow topology, the unsteadiness of the shock system and recirculation bubble in the trailing-edge region, as well as the sources of entropy generation.

Mean flow analysis shows that increasing the inlet Mach number shifts the SBLIs downstream on both the suction and pressure sides of the blade. For the $M_\infty = 1.85$ and 2.15 cases, the downstream displacement of the suction-side SBLI causes its shock-induced separation bubble to merge with the trailing-edge recirculation region. This merging yields a significantly thicker upper shear layer, displacing the sonic line away from the bubble and consequently shifting the upper trailing-edge shock outward. Analysis of unsteady flow features reveals that pressure fluctuations intensify with the presence of an SBLI near the trailing edge. For all Mach number cases, pronounced pressure RMS levels are observed along the trailing-edge shocks and shear layers, especially near the shock foot. Moreover, elevated turbulent kinetic energy develops along the shear layers, with peak values localized in the upper shear layer downstream of the trailing-edge bubble, where the magnitude increases with the inlet Mach number.

Spectral analysis indicates that the unsteadiness of the trailing-edge shocks is associated with low- and mid-frequency content ($St_c < 3.0$), and that increasing M_∞ from 1.85 to 2.15 systematically shifts this dominant unsteadiness toward lower frequencies. This shift, which is particularly evident along the lower trailing-edge shock, is likely related to the larger separation bubble formed near the trailing edge at $M_\infty = 2.15$. Furthermore, the characteristic frequencies of the trailing-edge bubble are highly sensitive to the inlet Mach number. The most energetic frequencies observed in the $M_\infty = 1.85$ case are associated with mid-frequency content ($St_c \approx 2.0$–3.0), whereas for the higher Mach numbers, the unsteadiness is governed by low-frequency dynamics ($St_c < 1.2$), featuring dominant peaks similar to those excited by the suction-side SBLI and the upper trailing-edge shock.

Analysis of the bubble dynamics reveals a strongly asymmetric mass flux over the surface of the trailing-edge separation bubble. For all Mach numbers, the suction-side bubble interface exhibits larger mass-flux magnitudes than that on the pressure-side, with mass ejection occurring predominantly near the trailing-edge apex and entrainment becoming dominant farther downstream, close to the bubble closure. These mass-flux processes are closely related to the breathing of the trailing-edge bubble, which in turn is dynamically coupled with the motion of the trailing-edge shock system. Time-correlation analysis reveals that variations in the bubble area precede the corresponding shock response. For the $M_\infty = 2.15$ case, where a large

shock-induced separation bubble forms near the trailing edge, the upper and lower shocks exhibit strongly synchronized motion.

Wake flow analysis indicats that higher Mach numbers amplify the pressure and density asymmetry between the suction and pressure surfaces near the trailing edge, causing a deflection of the wake toward the suction side (the lower-pressure and lower-density region). In addition, increasing the Mach number transitions the wake from a fully subsonic regime at $M_\infty = 1.85$ to a localized supersonic flow that decelerates back to subsonic speeds due to shock-turbulence interactions. Spectral proper orthogonal decomposition of the near-wake region identifis Kelvin-Helmholtz-type coherent structures associated with higher frequencies ($St_c > 7.0$). As the frequency increases, these coherent structures exhibit shorter spatial wavelengths. Overall, the topology of the wake modes is preserved for the different Mach numbers, suggesting that the fundamental instability mechanism remains robust within the investigated regime.

Finally, an entropy generation analysis shows that viscous dissipation dominates over irreversible heat transfer across all Mach number cases. The suction-side boundary layer acts as the primary source of aerodynamic losses, accounting for 50% to 58% of the total entropy generation, followed by the pressure-side boundary layer (35% to 38%). Notably, in contrast to typical subsonic turbine flows, the wake region contributes a relatively minor fraction (6% to 12%) to the overall entropy generation. This disparity is attributed to the severe velocity gradients present within the supersonic boundary layers along the blade surfaces, which dictate the overall loss generation.

Acknowledgements. H.F.S.L. and W.R.W. acknowledge Fundação de Amparo à Pesquisa do Estado de São Paulo, FAPESP, for supporting the present work under research grants No. 2013/08293-7, No. 2019/26196-5, No. 2021/14199-0, No. 2021/06448-0, and and No. 2025/13174-4. W.R.W. and H.F.S.L. also acknowledge the financial support from the Air Force Office of Scientific Research, AFOSR, for supporting the present work under grant FA9550-23-1-0615. We thank the Coaraci Supercomputer for computer time (FAPESP grant No. 2019/17874-0) and the Center for Computing in Engineering and Sciences at UNICAMP.

Conflict of interest. The authors declare that they have no conflict of interest.

References

[1] Denton, J.D.: The 1993 IGTI Scholar Lecture: Loss Mechanisms in Turbomachines. Journal of Turbomachinery **115**(4), 621–656 (1993)

[2] Sandberg, R.D., Michelassi, V.: Fluid dynamics of axial turbomachinery: Blade- and stage-level simulations and models. Annual Review of Fluid Mechanics **54**(1), 255–285 (2022)

[3] Nash, J.F., Quincey, V.G., Callinan, J.: Experiments of two-dimensional base flow at subsonic and transonic speeds. Technical Report 3427, Aeronautical Research Council (1963)

[4] Sieverding, C.H., Richard, H., Desse, J.-M.: Turbine blade trailing edge flow characteristics at high subsonic outlet mach number. Journal of Turbomachinery **125**(2), 298–309 (2003)

[5] Paniagua, G., Yasa, T., Loma, A., Castillon, L., Coton, T.: Unsteady strong shock interactions in a transonic turbine: Experimental and numerical analysis. Journal of Propulsion and Power **24**(4),

722–731 (2008)

[6] Melzer, A.P., Pullan, G.: The role of vortex shedding in the trailing edge loss of transonic turbine blades. Journal of Turbomachinery **141**(4), 041001 (2019)

[7] Sieverding, C., Manna, M.: A review on turbine trailing edge flow. International Journal of Turbomachinery, Propulsion and Power **5**(2) (2020)

[8] Rossiter, A.D., Pullan, G., Melzer, A.P.: The influence of boundary layer state and trailing edge wedge angle on the aerodynamic performance of transonic turbine blades. Journal of Turbomachinery **145**(4), 041008 (2022)

[9] Miki, K., Ameri, A., Giel, P.: Large eddy simulation analysis of loss anomaly of a turbine blade with large trailing edge radius. Journal of Turbomachinery **147**(3), 031012 (2024)

[10] Bienner, A., Gloerfelt, X., Cinnella, P.: Investigation of transonic flows through an idealized orc turbine vane using delayed detached eddy simulations. Applied Thermal Engineering **261**, 124951 (2025)

[11] Paniagua, G., Iorio, M.C., Vinha, N., Sousa, J.: Design and analysis of pioneering high supersonic axial turbines. International Journal of Mechanical Sciences **89**, 65–77 (2014)

[12] Herrin, J.L., Dutton, J.C.: Supersonic base flow experiments in the near wake of a cylindrical afterbody. AIAA Journal **32**(1), 77–83 (1994)

[13] Herrin, J.L., Dutton, J.C.: Supersonic near-wake afterbody boattailing effects on axisymmetric bodies. Journal of Spacecraft and Rockets **31**(6), 1021–1028 (1994)

[14] Herrin, J.L., Dutton, J.C.: Effect of a rapid expansion on the development of compressible free shear layers. Physics of Fluids **7**(1), 159–171 (1995)

[15] Scarano, F., Van Oudheusden, B.: Planar velocity measurements of a two-dimensional compressible wake. Experiments in Fluids **34**, 430–441 (2003)

[16] Janssen, J.R., Dutton, J.C.: Time-series analysis of supersonic base-pressure fluctuations. AIAA Journal **42**(3), 605–613 (2004)

[17] Humble, R.A., Scarano, F., Oudheusden, B.W.: Unsteady flow organization of compressible planar base flows. Physics of Fluids **19**(7), 076101 (2007)

[18] Yang, R., Wang, Z.-g., Wu, J.-p.: Instability of an asymmetric supersonic planar wake. Acta Astronautica **173**, 86–90 (2020)

[19] Kirchner, B.M., Favale, J.V., Elliott, G.S., Dutton, J.C.: Three-component turbulence measurements and analysis of a supersonic, axisymmetric base flow. AIAA Journal **57**(6), 2496–2512 (2019)

[20] Kirchner, B.M., Elliott, G.S., Dutton, J.C.: Coherent turbulence and entrainment in a supersonic,

axisymmetric, separated/reattaching shear layer. Phys. Rev. Fluids **5**, 084605 (2020)

[21] Kirchner, B.M., Elliott, G.S., Dutton, J.C.: Three-dimensional flow structure in an axisymmetric separated/reattaching supersonic flow. Phys. Rev. Fluids **6**, 024604 (2021)

[22] Simon, F., Deck, S., Guillen, P., Sagaut, P., Merlen, A.: Numerical simulation of the compressible mixing layer past an axisymmetric trailing edge. Journal of Fluid Mechanics **591**, 215–253 (2007)

[23] Sandberg, R.D.: Numerical investigation of turbulent supersonic axisymmetric wakes. Journal of Fluid Mechanics **702**, 488–520 (2012)

[24] Saracoglu, B.H., Paniagua, G., Sanchez, J., Rambaud, P.: Effects of blunt trailing edge flow discharge in supersonic regime. Computers & Fluids **88**, 200–209 (2013)

[25] Martinez-Cava, A., Wang, Y., Vicente, J.d., Valero, E.: Pressure bifurcation phenomenon on supersonic blowing trailing edges. AIAA Journal **57**(1), 153–164 (2019)

[26] Stack, C.M.: Turbulence mechanisms in a supersonic rectangular multistream jet with an aft-deck. PhD thesis, The Ohio State University (2019)

[27] Doshi, P.S., Gaitonde, D.V., Gist, E.D., Glauser, M.N.: Passive control of supersonic shear layer in rectangular multistream jet. AIAA Journal **60**(10), 5692–5706 (2022)

[28] Lui, H.F.S., Wolf, W.R., Ricciardi, T.R., Gaitonde, D.V.: Mach number effects on shock-boundary layer interactions over curved surfaces of supersonic turbine cascades. Theoretical and Computational Fluid Dynamics **38**, 451–478 (2024)

[29] Lui, H.F.S., Ricciardi, T.R., Wolf, W.R., Braun, J., Rahbari, I., Paniagua, G.: Unsteadiness of shock-boundary layer interactions in a Mach 2.0 supersonic turbine cascade. Phys. Rev. Fluids **7**, 094602 (2022)

[30] Liu, Z., Braun, J., Paniagua, G.: Characterization of a supersonic turbine downstream of a rotating detonation combustor. Journal of Engineering for Gas Turbines and Power **141**(3), 031501 (2019)

[31] Nagarajan, S., Lele, S.K., Ferziger, J.H.: A robust high-order compact method for large eddy simulation. Journal of Computational Physics **191**(2), 392–419 (2003)

[32] Lele, S.K.: Compact finite difference schemes with spectral-like resolution. Journal of Computational Physics **103**(1), 16–42 (1992)

[33] Mathew, J., Lechner, R., Foysi, H., Sesterhenn, J., Friedrich, R.: An explicit filtering method for large eddy simulation of compressible flows. Physics of Fluids **15**(8), 2279–2289 (2003)

[34] Kawai, S., Shankar, S.K., Lele, S.K.: Assessment of localized artificial diffusivity scheme for large-eddy simulation of compressible turbulent flows. Journal of Computational Physics **229**(5), 1739–1762 (2010)

[35] Bhaskaran, R., Lele, S.K.: Large eddy simulation of free-stream turbulence effects on heat transfer to a high-pressure turbine cascade. Journal of Turbulence **11**, 6 (2010)

[36] Waindim, M., Gaitonde, D.V.: A body-force based method to generate supersonic equilibrium turbulent boundary layer profiles. Journal of Computational Physics **304**, 1–26 (2016)

[37] Poinsot, T.J., Lele, S.K.: Boundary conditions for direct simulations of compressible viscous flows. Journal of Computational Physics **101**(1), 104–129 (1992)

[38] Georgiadis, N.J., Rizzetta, D.P., Fureby, C.: Large-eddy simulation: Current capabilities, recommended practices, and future research. AIAA Journal **48**(8), 1772–1784 (2010)

[39] Loginov, M.S., Adams, N.A., Zheltovodov, A.A.: Large-eddy simulation of shock-wave/turbulent-boundary-layer interaction. Journal of Fluid Mechanics **565**, 135–169 (2006)

[40] Touber, E., Sandham, N.D.: Large-eddy simulation of low-frequency unsteadiness in a turbulent shock-induced separation bubble. Theoretical and Computational Fluid Dynamics **23**, 79–107 (2009)

[41] Agostini, L., Larchevêque, L., Dupont, P., Debiève, J.-F., Dussauge, J.-P.: Zones of influence and shock motion in a shock/boundary-layer interaction. AIAA Journal **50**(6), 1377–1387 (2012)

[42] Adler, M.C., Gaitonde, D.V.: Dynamic linear response of a shock/turbulent-boundary-layer interaction using constrained perturbations. Journal of Fluid Mechanics **840**, 291–341 (2018)

[43] Lui, H.F.d.S., Wolf, W.R.: Interplay between streaks and vortices in shock-boundary layer interactions with conditional bubble events over a turbine airfoil. Phys. Rev. Fluids **11**, 013401 (2026)

[44] Hamada, G.Y.R., Wolf, W.R., Lui, H.F.S., Junqueira-Junior, C.: Characterization of supersonic boundary layers of adiabatic and isothermal curved surfaces with shock interactions. International Journal of Heat and Fluid Flow **117**, 110029 (2026)

[45] Pantano, C., Sarkar, S.: A study of compressibility effects in the high-speed turbulent shear layer using direct simulation. Journal of Fluid Mechanics **451**, 329–371 (2002)

[46] Rao, S.M.V., Asano, S., Imani, I., Saito, T.: Effect of shock interactions on mixing layer between co-flowing supersonic flows in a confined duct. Shock Waves **28**(2), 267–283 (2018)

[47] Spina, E.F., Smits, A.J., Robinson, S.K.: The physics of supersonic turbulent boundary layers. Annual Review of Fluid Mechanics **26**(1), 287–319 (1994)

[48] Fang, J., Zheltovodov, A.A., Yao, Y., Moulinec, C., Emerson, D.R.: On the turbulence amplification in shock-wave/turbulent boundary layer interaction. Journal of Fluid Mechanics **897**, 32 (2020)

[49] Holzner, M., Lüthi, B.: Laminar superlayer at the turbulence boundary. Phys. Rev. Lett. **106**, 134503 (2011)

[50] Jahanbakhshi, R., Madnia, C.K.: Entrainment in a compressible turbulent shear layer. Journal of Fluid Mechanics **797**, 564–603 (2016)

[51] Towne, A., Schmidt, O.T., Colonius, T.: Spectral proper orthogonal decomposition and its relationship to dynamic mode decomposition and resolvent analysis. Journal of Fluid Mechanics **847**, 821–867 (2018)

[52] Chu, B.T.: On the energy transfer to small disturbances in fluid flow (part i). Acta Mechanica **1**, 215–234 (1965)

[53] Rajaee, M., Karlsson, S.K.F., Sirovich, L.: Low-dimensional description of free-shear-flow coherent structures and their dynamical behaviour. Journal of Fluid Mechanics **258**, 1–29 (1994)

[54] Ribeiro, J.H.M., Wolf, W.R.: Identification of coherent structures in the flow past a NACA0012 airfoil via proper orthogonal decomposition. Physics of Fluids **29**(8), 085104 (2017)

[55] Cantwell, B.: Fundamentals of Compressible Flows, Stanford, CA (2022)

[56] Wheeler, A.P.S., Sandberg, R.D., Sandham, N.D., Pichler, R., Michelassi, V., Laskowski, G.: Direct numerical simulations of a high-pressure turbine vane. Journal of Turbomachinery **138**(7), 071003 (2016)

[57] Zhao, Y., Sandberg, R.D.: Using a new entropy loss analysis to assess the accuracy of RANS predictions of an high-pressure turbine vane. Journal of Turbomachinery **142**(8), 081008 (2020)

[58] Lopes, G., Tene Hedje, P., Bricteux, L., Lavagnoli, S., Dellacasagrande, M., Przytarski, P., Lengani, D.: Breakdown of the entropy transport terms in a high-speed low-pressure turbine. Journal of Turbomachinery **148**(9), 091012 (2026)

Supplementary Files

This is a list of supplementary files associated with this preprint. Click to download.

- movie1.mp4
- movie2.mp4
- movie3.mp4